# Machine-learning-based Reduced-Order Modelling of a morphing wing in turbulent flow using Proper Orthogonal Decomposition and mesh deformation

Abderahmane Marouf, Nils Maynard, Rajaa El Akoury, Jean-François Rouchon, Yannick Hoarau, Marianna Braza

International Journal of Heat and Fluid Flow 120 (2026) 110380

Contents lists available at ScienceDirect

International Journal of Heat and Fluid Flow

journal homepage: www.elsevier.com/locate/ijhff

# Machine-learning-based Reduced-Order Modelling of a morphing wing in turbulent flow using Proper Orthogonal Decomposition and mesh deformation☆

Abderahmane Marouf[a,*], Nils Maynard[b,c], Rajaa El Akoury[b], Jean-François Rouchon[c], Yannick Hoarau[a], Marianna Braza[b]

[a] University of Strasbourg, ICUBE UMR 7357, Laboratoire des Sciences de l'Ingénieur, de l'Informatique et de l'Imagerie, France
[b] IMFT Institut de Mécanique des Fluides de Toulouse, Unité Mixte C.N.R.S.-I.N.P.T. 5502, All. du Prof. Camille Soula, 31400 Toulouse, France
[c] LAPLACE - Laboratoire Plasma et Conversion d'Energie, UMR 5213 CNRS-INPT-UT3, France

ARTICLE INFO

*Keywords:*
POD
LSTM
Machine learning
Aerodynamics
Morphing

ABSTRACT

This study introduces a novel approach to predict the turbulent flow dynamics around morphing wings, specifically focusing on the flow around an Airbus A320 airfoil at a Reynolds number of 1 million and an angle of attack (10°). The flow exhibits detachment near 70% of the chord. The proposed method uses an extended Proper Orthogonal Decomposition (POD) mesh-based approach, accounting for real-time wing deformation according to a Travelling Wave (TW) to manipulate flow separation and wake instabilities. The POD is coupled with Machine Learning models, particularly Long Short-Term Memory (LSTM), allowing for extension of the Hi-Fi solution over a longer physical time rapidly. The results are compared to the High-Fidelity approach. The relative error is less than 3% located further downstream in the wake. The study compares several model architectures such as standard and Bidirectional LSTM, ultimately proposing a Hybrid model associating a POD reconstruction to the best LSTM architecture with both models that demonstrates high accuracy in predicting time averaged and unsteady velocity fields based in the wake compared to the other models.

## 1. Introduction

Global warming, climate change, and environmental pollution have become major, interrelated challenges threatening life on Earth. As atmospheric $CO_2$ accumulates, it traps infrared radiation emitted by the planet's surface, thereby amplifying the greenhouse effect and driving global warming (Zandalinas et al., 2021). The European Commission has outlined a policy framework aimed at achieving climate neutrality by 2050, which includes an interim objective of reducing net greenhouse gas emissions by 55% by the year 2030 (https://commission.europa.eu/energy-climate-change-environment_en). Industry initiatives have improved fuel efficiency, yielding up to a 24% reduction in fuel burned per passenger between 2005 and 2017. However, these gains have been largely offset by the substantial growth in air travel over the same period. By 2017, passengers were flying on average 60% farther than they did in 2005, diminishing the net environmental benefits of improved efficiency. Aviation accounted for approximately 3.8% of total EU-28 greenhouse-gas (GHG) emissions in 2017, making it the second-largest source of emissions within the transport sector after road transport. However, it represented about 13–14% of the transport sector's emissions, which highlights the disproportionate impact of aviation on climate despite its relatively smaller share of overall GHG emissions. (https://www.eea.europa.eu).

Multiple strategies have been proposed to reduce fuel consumption by enhancing the aerodynamic efficiency of aircraft, including the development of novel designs and advanced optimization approaches. However, achieving these improvements typically relies on high-fidelity computational simulations, which demand substantial computational resources and access to High-Performance Computing (HPC) infrastructures. These requirements often limit the pace and cost-effectiveness of design exploration. Unsteady high-fidelity simulations for turbulent flows are usually time consuming, contain non-linear dynamics, separations, instabilities, shear-layers and wake development such as flows around wings. The optimization of these conditions such as

☆ This article is part of a special issue entitled: 'AERO2025' published in International Journal of Heat and Fluid Flow.

* Corresponding author.
*E-mail address:* amarouf@unistra.fr (A. Marouf).

https://doi.org/10.1016/j.ijheatfluidflow.2026.110380
Received 30 November 2025; Received in revised form 14 February 2026; Accepted 16 March 2026
Available online 20 March 2026

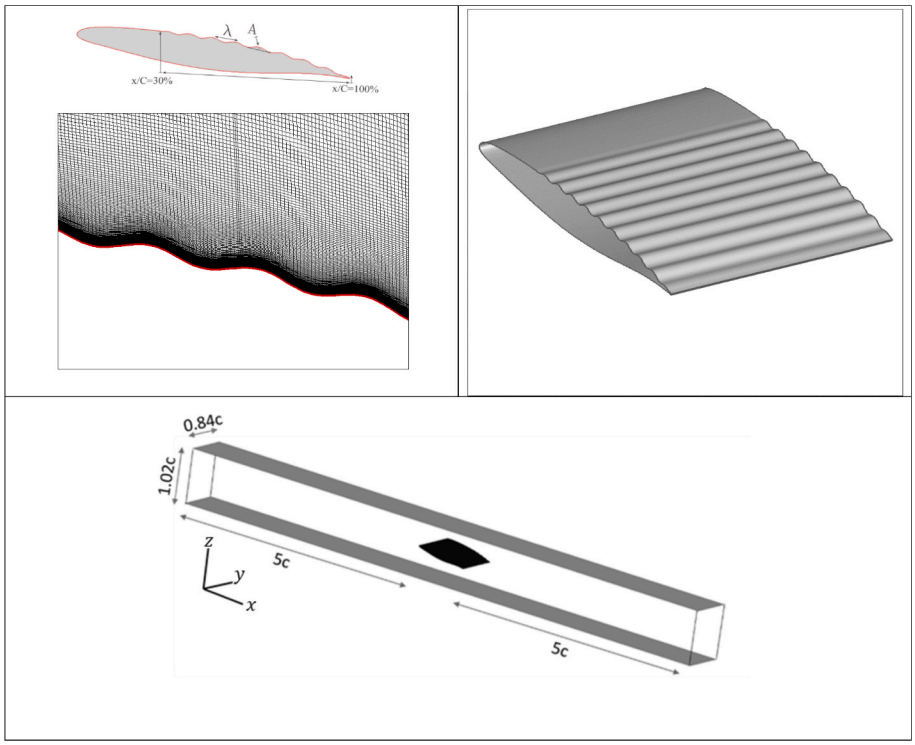


**Fig. 1.** Illustration of the Travelling Wave (TW) concept implemented on the so-called "Intermediate Scale – IS" A320 morphing wing prototype of the BEALIVE project having a chord of 70 cm, approximately 1/4 of the real swept wing chord near half-span. On the left, presentation of the mesh deformation. (Down): presentation of the boundary conditions and the flow domain.

reducing or delaying the separation were investigated by (Truong et al., 2023). This study has shown a drag decrease. Manipulation of the shear-layers leading to reduction of the wake drag and attenuation of instabilities leading to an improvement of the wing's performances have been widely studied by the morphing research studies (Tô et al., 2019, Simiriotis et al., 2019, and Marouf et al., 2021, 2023). More recently, traveling waves for transonic speed under buffet conditions (Abou Khalil et al., 2024) has shown that an important reduction of the drag could be achieved through the manipulation of the shock wave position under the effect of a travelling wave.

Since parametric studies are challenging and time consuming, many researchers have focused on developing new simulation models with Machine Learning algorithms coupled with High-Fidelity (Hi-Fi) simulation to replace traditional models, to conduct optimization with less demanding time and faster CFD. Machine Learning has the potential to improve CFD and to speed up the Hi-Fi simulations, enhance and develop turbulence models, and elaborate a new family of Reduced Order Models for several areas such as experimental measurements, flow control applications, and other fields. Direct Numerical Simulation (DNS) requires a very fine grid to capture all degrees of freedom and to resolve all the flow structures with their multi-scale energy distribution.

Deep learning models were proposed to improve the DNS efficiency (Bar-Sinai et al., 2019), such as improving high order schemes (Stevens and Colonius, 2020a), or by using coarser grids (Li et al., 2020). (Stevens and Colonius, 2020b), used full-convolutional with long short-term memory (LSTM), (Hochreiter and Schmidhuber, 1997) to enhance the accuracy of discretization methods. In the context of Reynolds Averaged Navier Stokes (RANS) simulations, recent studies have shown that deep learning could be used for RANS modelling and outperforms in some cases classical RANS models (Ling et al., 2016, and Kutz, 2017).

Recently, Physics-informed NNs (PINNs) demonstrated their ability to solve the RANS equations without any specific model or assumption for turbulence and using data on the domain boundaries showing good accuracy of Reynolds-stress components (Eivazi et al., 2022). CNNs are also used in LES modelling for subgrid-scale (SGS) models (Beck et al., 2019; Lapeyre et al., 2019). The application of neural networks for high-fidelity simulations, such as training models with hundreds of thousands or even millions of volume cells for a single parameter such as velocity or pressure fields over an extended simulation period, can lead to prolonged training times. This fact may be impractical for parametric or optimization processes.

ROM modelling is employed together with Machine Learning algorithms to better improve the Hi-Fi simulations prediction. Proper Orthogonal Decomposition (POD) projects high-dimensional non-linear simulations data to an orthogonal vector of eigenmodes in a low-dimensional level, allowing building the Reduced Order Model (ROM). The POD has been applied to turbulent flows by (Lumley, 1967), The work of (Sirovich, 1987) developed the separable POD in respect of space and time through the snapshot method involving a construction of time series matrix, calculation of a correlation matrix and its related eigen values and vectors. The objective of construction Reduced Order Models (ROMs) is to avoid the resolution of the full system of Navier-Stokes equations in intermediate parameters of a large parametric space. ROMs have been derived for optimization of flows such as flow control systems, because of their low cost of computation and efficiency to construct control system. The POD provides spatial and temporal modes organized from high to low dominant energy. The use of Machine Learning employing various types of Neural Networks (NNs) such as the feedforward, conventional and recurrent types promise an important achievement together with the POD.

(Mohan and Gaitonde, 2018) considered two-dimensional flows using a very short spatial window for training and used a deep learning-based approach to build a ROM using the POD basis of canonical DNS datasets. (Maulik et al., 2021) proposed a new model based on Convolutional AutoEncoders (CAE)-LSTM method and compared it to the POD Galerkin Projection (GP), they focused on flows without bluff bodies, thus excluding shear layers, wake instabilities, and flow separation, and limited their study to Reynolds numbers up to 4000. (Du

et al., 2024) employed encoder–decoder architectures based on CNNs and Convolutional LSTMs to predict flow fields, without using any POD-based reduced-order modelling. The focus of this study is related to the application of the Long Short-Term Memory LSTM (Hochreiter and Schmidhuber, 1997) due to its predictive ability of time dependent systems compared to classical Recurrent NNs. The use of LSTM-POD in turbulent flows and their reconstruction with the learning ability of LSTM has been shown by (Deng et al., 2019) with experimental time-resolved PIV velocity fields. The developed model provided better performance with high accuracy and low relative reconstruction errors. A comparison between various types of LSTM has shown that over-fitting problem is caused for the application of modelling complex sequential data for turbulent flow and flow control applications by Mohan and Gaitonde (2018). Application to wind farms for unsteady fluid systems was proposed by Zhang and Zhao (2020). The developed model was able to predict the unsteady turbines wakes with an acceptable error compared to the Hi-Fi simulation.

The present study introduces a novel framework for Fluid–Structure Interaction (FSI) problems with application to morphing wings, combining Proper Orthogonal Decomposition (POD) with Machine Learning techniques based on Long Short-Term Memory (LSTM) neural networks. The approach enables the prediction of unsteady flow phenomena, such as trailing-edge separation and wake dynamics, while accounting for the interaction with a deformable wing and real-time mesh deformation. The POD methodology is extended to include mesh motion. Several LSTM architectures are evaluated and compared to the Hi-Fi simulations to assess their accuracy and robustness.

## 2. Physical parameters

### 2.1. Case of morphing with traveling wave

Within the framework of the HORIZON-2023-2027-PATHFINDER Project N° 101129952-BEALIVE-"Bioinspired Electroactive multiscale Aeronautical Live skin", http://horizon-europe-bealive.eu/ and https://cordis.europa.eu/project/id/101129952, our research group is investigating the implementation of an innovative "live skin" concept on a strategic part of the suction side of the wing. This morphing concept, realised experimentally by a high Degree of Freedom (DoF) of piezo-actuators, creates a Travelling Wave (TW) actuation mechanism that has been implemented in the CFD code NSMB (Navier-Stokes Multi-Block, (Vos et al, 1998, Hoarau, 2002)). The mesh deformation is handled by Arbitrary Lagrangian Eulerian (ALE), (Donea et al, 1982), as illustrated in Fig. 1.

The main parameters of the Travelling Wave (TW) are the frequency, amplitude, wavelength and location of the actuation zone. Optimal ranges have been determined through a large parametric study (El Akoury et al., 2024). In this study, our focus only on a fixed configuration with an amplitude (A) of 0.15% of the total chord. The wavelength ($\lambda$) is fixed to 8.5% of the total chord close the wavelength of the upper shear layer. The actuation frequency is set to 300 Hz, which proved optimality from trailing-edge actuations studies (Marouf et al., 2021). The starting point of the Travelling Wave is set at 30% of the chord until the end of the trailing-edge.

$$Z(x,t)=\begin{cases}\dfrac{x-x_0}{x_1-x_0}A\sin(kx-\omega t+\phi)\ \text{if}\ x\in[x_0,x_1]\\ A\sin(kx-\omega t+\phi)\ \text{if}\ x\in[x_0,x_1]\\ \dfrac{x_f-x}{x_f-x_2}A\sin(kx-\omega t+\phi)\ \text{if}\ x\in[x_2,x_f]\end{cases}\tag{1}$$

$k$ is the wave number ($2\pi/\lambda$), the $\omega$ is the angular frequency ($2\pi f_{tw}$) calculated from the imposed wave frequency ($f_{tw}$). An appropriate smoothing has been applied to the extremities of the travelling wave between $x_0-x_1$ and $x_2-x_f$ to avoid sharp deformation and cells distortion.

### 2.2. Governing equations and turbulence model

The simulations over the A320 aerofoil have been accomplished by using the Navier-Stokes Multi Block (NSMB) code, recent development of turbulence modelling could be found in Marouf et al. (Marouf et al., 2025). The Navier-Stokes equations are solved for compressible flows. A preconditioning method based on artificial compressibility was employed within our compressible solver, NSMB, using the implicit dual time-stepping approach combined with the Lower–Upper Symmetric Gauss–Seidel (LU-SGS) scheme. For the spatial discretization, a second-order central scheme was employed for the diffusive terms, while a fourth-order standard central skew-symmetric scheme supplemented with artificial dissipation terms (Jameson, 1993) was used for the convective terms. The grid resolution ensures that the $y^+$ values remain below 0.5 throughout the near-wall region, thereby guaranteeing optimal performance of the near-wall turbulence modelling.

The finite volume method is employed on multi-block structured grids, using Message Passing Interface (MPI) for parallel simulations. The continuity and momentum equations, according to Favre (Favre, 1983) averaging in respect of the compressibility and in cartesian coordinates are expressed in their conservative form as follows:

$$\frac{\partial\overline{\rho}}{\partial t}+\frac{\partial}{\partial x_i}\left(\overline{\rho}\widetilde{u_i}\right)=0\tag{2}$$

$$\frac{\partial}{\partial t}\left(\overline{\rho}\widetilde{u_i}\right)+\frac{\partial}{\partial x_j}\left(\overline{\rho}\widetilde{u_j}\widetilde{u_i}\right)=-\frac{\partial\overline{p}}{\partial x_i}+\frac{\partial}{\partial x_j}\left(\widetilde{\tau}_{ij}-\overline{\rho}\widetilde{u_j''u_i''}\right)\tag{3}$$

$$\begin{aligned}\frac{\partial}{\partial t}\left(\overline{\rho}\widetilde{E}+\frac{\overline{\rho}\widetilde{u_j''u_i''}}{2}\right)+\frac{\partial}{\partial x_j}\left(\overline{\rho}\widetilde{u_j}\widetilde{H}+\widetilde{u_j}\frac{\overline{\rho}\widetilde{u_j''u_i''}}{2}\right)&=\frac{\partial[\widetilde{u_i}(\widetilde{\tau}_{ij}-\overline{\rho}\widetilde{u_j''u_i''})]}{\partial x_j}\\&+\frac{\partial(\overline{q_j}-\overline{\rho}\widetilde{u_j''H''}+\widetilde{\tau_{ij}u_i''}-\frac{1}{2}\overline{\rho}\widetilde{u_j''u_i''u_i''})}{\partial x_j}\end{aligned}\tag{4}$$

where:

$$\overline{p}=\overline{\rho}r\widetilde{T}\ \text{and}\ \overline{\rho}\widetilde{u_i}=\overline{\rho}\widetilde{u_i}\tag{5}$$

$$t_{ij}=-\overline{\rho}\widetilde{u_j''u_i''}\tag{6}$$

$t_{ij}$*is* the Favre-averaged Reynolds stress tensor.

The turbulence modelling approached used is the organised Eddy Simulation (OES) sensitised to capture the coherent structures development (Braza et al., 2006, Bourguet et al., 2008, Szubert et al., 2015), able to predict correctly the coherent structure dynamics and the related flow instabilities as presented in the following.

In the configuration shown in Fig. 1, a fixed-velocity inlet is set as an inflow condition. The present configuration corresponds to an internal (confined) flow that respects the dimensions of the S4 wind tunnel of IMFT in which experimental results are conducted too. Regarding the walls, both slip and no-slip boundary conditions were tested, and their influence on the flow was found to be negligible. The slip condition was therefore adopted to avoid resolving boundary layers near the walls, which could otherwise slightly affect the flow around the airfoil due to the confined geometry (i.e., the small distance between the airfoil and the walls). Concerning the computational domain horizontal dimension, a careful study was undertaken to avoid any feedback effect from artificial confinement at the outlet boundary, where non-reflecting boundary conditions have been used inspired from (Jin & Braza, 1993), applied to low subsonic/incompressible flows as well as (Poinsot & Lele, 1992), for compressible flows formulation.

These facts prevent pressure feedback effects from the outlet boundary towards the inner region. Corrections at the outlet, result in a smoother residual evolution and improved robustness of the solution procedure.

This type of outlet condition is particularly well suited for confined

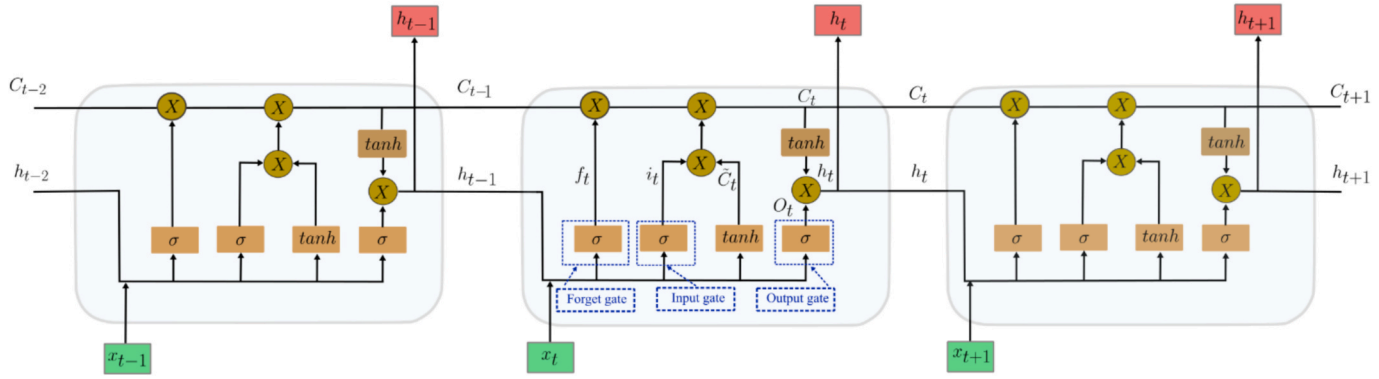


**Fig. 2.** Illustration of the LSTM network architecture with a multi-time-step model.

internal flows, where artificial boundaries are introduced and the outlet pressure must adapt dynamically to the internal flow development. The lateral boundaries are defined as symmetry planes.

### 2.3. Proper orthogonal decomposition with mesh deformation

To analyse the dynamics of the wake coherent structures and to reduce the large number of degrees handled by the Hi-Fi simulations, the POD has been applied. The mesh deformation has been handled using the Arbitrary Lagrangian Eulerian (ALE) (Donea et al, 1982) to maintain a similar mesh topology when the Travelling Wave is activated. The solution state vector including the mesh deformation and the flow state variables such as velocity and pressure fields is defined as $\boldsymbol{s}(\boldsymbol{x},\boldsymbol{t})$ and can be written as follows:

$$\boldsymbol{s}(\boldsymbol{x},\boldsymbol{t}) = \begin{pmatrix} \chi_i(\boldsymbol{x},\boldsymbol{t}) \\ \rho(\boldsymbol{x},\boldsymbol{t}) \\ \mathbf{v}_i(\boldsymbol{x},\boldsymbol{t}) \\ p(\boldsymbol{x},\boldsymbol{t}) \end{pmatrix} \quad \textbf{with } \boldsymbol{i} = 1,\ 2,\ 3 \tag{7}$$

where $\rho, v_i$ and $p$ are the density, the three components of the velocity, and the pressure. A series of snapshots is collected from the Hi-Fi simulations. The state vector is decomposed using Reynolds decomposition to the statistical mean and fluctuating part, as follows, where the fluctuating part is decomposed through the POD to a series of spatial modes multiplied by the temporal coefficients:

$$s_i(x,t) = \langle s_i(x)\rangle + s_i'(x,t) = \langle s_i(x)\rangle + \sum_{j=1}^{\infty} \phi_j^{s_i}(x) a_j^{s_i}(t) \tag{8}$$

The term $s_i'(x,t)$ denotes the fluctuation beyond the mean, according to the Reynolds decomposition. It is assumed that the flow solution is statistically steady. The unsteady part of the state vector in Eq. (8) can also be described using time-invariant POD spatial modes $\phi_j^{s_i}(x)$ and spatially invariant POD temporal modes $a_j^{s_i}(t)$. The approximated solution of the state vector employs a reduced number of energy dominant POD modes $\phi_j^{s_i}(x)$ and their associated time coefficients $a_j^{s_i}(t)$, as illustrated in the following equation:

$$s_i(x,t) \approx \langle s_i(x)\rangle + \sum_{j=1}^{N_r^{s_i}} \phi_j^{s_i}(\boldsymbol{x}) a_j^{s_i}(t) \qquad t_1 \le t \le t_{sn} \tag{9}$$

A reduced-order solution can be derived for the time interval during which snapshots are collected specifically from $t_1 to t_{sn}$. In this context, $\boldsymbol{N_r^{s_i}}$ denotes the reduced number of POD modes for $s_i$, which may vary for each variable of the solution state vector. Here, $t_1$ and $t_{sn}$ represent the times of the first and last snapshots, respectively. Let's $R$ be the two-point time-correlation function, defined as follows:

$$R(\eta) = \begin{pmatrix} R^{\chi_i}{}_{(t_i \times t_j)} \\ \vdots \\ R^{\rho}{}_{(t_i \times t_j)} \\ \vdots \\ R^{p}{}_{(t_i \times t_j)} \\ \vdots \\ R^{v_{1,2,3}}{}_{(t_i \times t_j)} \end{pmatrix} = \frac{1}{N_t} \begin{pmatrix} \left((\chi_{1,2,3}(x,t_i), \chi_{1,2,3}(x,t_j)\right)_\Omega \\ \vdots \\ \left((\rho(x,t_i), \rho(x,t_j)\right)_\Omega \\ \vdots \\ \left((\mathrm{p}(x,t_i), \mathrm{p}(x,t_j)\right)_\Omega \\ \vdots \\ \left((v_{1,2,3}(x,t_i), v_{1,2,3}(x,t_j)\right)_\Omega \end{pmatrix} \tag{10}$$

where $N_t$ represents the number of snapshots used to estimate the time-correlation tensor. The subscript $(t_i \times t_j)$ indicated the dimensions of each element within the correlation tensor. The correlation tensor $R(\eta)$ is determined by solving an eigenvalue problem, as described in the following equation:

$$R^{s_i}\, a_j^{s_i}(t) = \lambda_j^{s_i}\, a_j^{s_i}(t) \tag{11}$$

where $\lambda_j^{s_i}$ represent the eigenvalues. The eigen functions $a_j^{s_i}(t)$ satisfy,

$$\left(a_j^{s_i}(t), a_k^{s_i}(t)\right)_{t_{sn}} = \delta_{jk} \tag{12}$$

where $\delta_{jk}$ is the Kronecker delta. The POD modes are organized in descending order based on their energy content (eigenvalues), such that $\lambda_1^{s_i} \ge \lambda_2^{s_i} \ge \ldots\ldots\ldots \ge \lambda_{N_{pod}}^{s_i} > 0$. The orthonormal POD spatial modes are derived ensuring that $\langle \phi_j^{s_i}(x), \phi_k^{s_i}(x)\rangle_\Omega = \delta_{jk}$ using the following equation:

$$\phi_j^{s_i}(x) = \frac{1}{\sqrt{N_t \lambda_j^{s_i}}} \left(s_i'(x,t),\ a_j^{si}(t)\right)_{t_{sn}} \tag{13}$$

The corresponding POD time coefficients are given by:

$$a_j^{s_i}(t) = \left(\phi_j^{s_i}(x),\ s_i'(x;t)\right)_\Omega = \sqrt{N_t \lambda_j^{s_i}}\, a_j^{s_i}(t) / \left|a_j^{s_i}(t)\right|_T \tag{14}$$

Generally, the number of reduced POD modes ($N_r^{s_i}$) is much smaller than the total number of POD modes ($N_r^{s_i} << N_{s_i}^{POD}$), under the condition that it captures most of the system energy.

### 2.4. Long-short term memory (LSTM)

The LSTM neural networks were specifically designed to address the exploding and vanishing gradient issues encountered during the training of transitional Recurrent Neural Networks (NNs). LSTM networks exhibit exceptional learning capabilities in handling classification and regression tasks based on time-series data. The fundamental structure of LSTM NNs is illustrated in Fig. 2. Each LSTM unit consists of the following multiplicative gates: the input, output, and forget gate. These gates enable the LSTM memory cell to retain and retrieve information

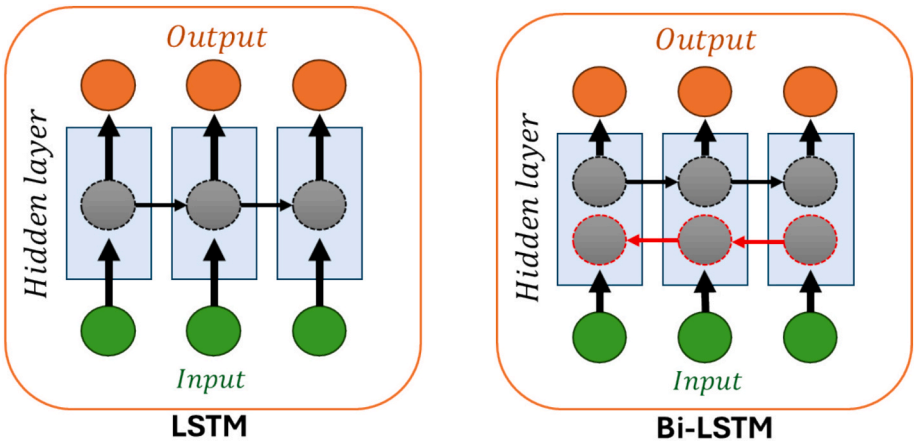


**Fig. 3.** Comparison of LSTM (Hochreiter and Schmidhuber, 1997) and Bi-LSTM, (Graves et al., 2005) architectures.

over extended periods, thereby decreasing the vanishing gradient issue.

The forget gate decides whether to discard or preserve information, acting similarly to memory processes. The equations for the LSTM at each time step are given by:

$$i_t = \sigma(W_i x_t + U_i h_{t-1} + b_i),$$

$$f_t = \sigma\left(W_f x_t + U_f h_{t-1} + b_f\right),$$

$$\widetilde{C}_t = \tanh(\mathrm{W_c} x_t + U_c h_{t-1} + b_c),$$

$$C_t = i_t \otimes \widetilde{C}_t + f_t \otimes C_{t-1},$$

$$O_t = \sigma(W_o x_t + U_o h_{t-1} + b_o),$$

$$h_t = O_t \otimes \tanh(C_t),$$

$x_t$ represents the cell input and $h_t$ denotes the cell output. The variables $f_t$ denotes the forget gate, $i_t$ the input gate and $O_t$ corresponds to the output gate. $C_t$ and $\widetilde{C}_t$ represent the cell state and its update respectively. The terms $W$ and $U$ refer to the weight matrices associated with different gates, and the $b$ terms are bias vectors. These weights and biases are learned during the training process. $\sigma$ is the logistic sigmoid function, and $\otimes$ denotes element-wise multiplication operator.

The conventional LSTM models sequential data using information

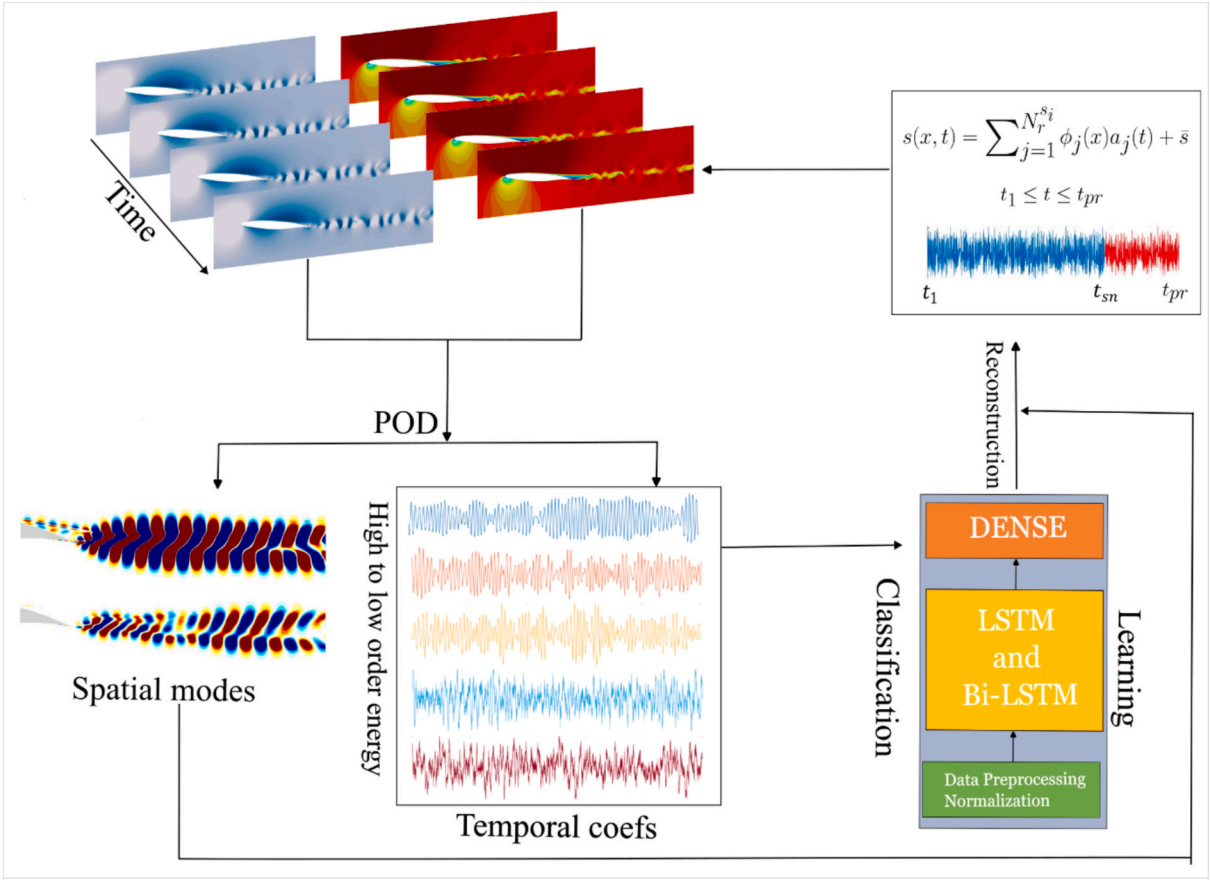


**Fig. 4.** Flow chart of POD with spatial and temporal modes decomposition with LSTM and Bi-LSTM with the reconstruction field for flow prediction.

**Table 1**
Sensitivity study of various grids in respect of the mean aerodynamic coefficients (lift and drag) for steady simulations.

| | Mesh 1 | Mesh 2 | Mesh 3 | Mesh 4 |
|---|---|---|---|---|
| Number of cells | 246 k | 276 k | 323 k | 362 k |
| $CL$ | 1.4918 | 1.5002 | 1.5018 | 1.5164 |
| $\left\|\frac{CL_{fine} - CL_i}{CL_{fine}} \times 100\right\|$ | 1.6244 | 1.0726 | 0.9652 | – |
| $CD$ | 0.0271 | 0.0270 | 0.0272 | 0.0267 |
| $\left\|\frac{CD_{fine} - CD_i}{CD_{fine}} \times 100\right\|$ | 1.5711 | 1.3735 | 0.3423 | – |

propagated in a single temporal direction. The Bidirectional LSTM employs two recurrent layers that process the sequence in forward and backward directions (Fig. 3). This architecture enables the model to exploit both preceding and subsequent temporal information within the sequence, thereby enhancing its ability to represent complex spatio-temporal dependencies.

The LSTM neural networks have been implemented using the open-source TensorFlow package (Abadi et al., 2016). TensorFlow offers a Python Application Program Interface (API) that provides access to a wide range of tensor and matrix operations, many of which are optimized for deep-learning applications. A widely used high-level wrapper "Keras" library, (Chollet et al., 2018), for TensorFlow that provides a concise interface and simplifies the neural-network construction. Combined with standard Python libraries for numerical modelling, such as NumPy and Matplotlib, these tools have been used to build a self-contained framework capable of importing datasets and constructing ROMs. The network architecture consists of two hidden layers; this intentionally shallow design enabled direct comparison with a Bidirectional LSTM (Bi-LSTM) of a similar structure while also reducing computational expense. Hyperparameters including the number of units, learning rate, and batch size were tuned using a random search strategy. The mean absolute error has been selected as the loss function, and the Adam (Adaptive Moment Estimation) optimizer was found to deliver superior performance. All reported results have been obtained from an ensemble of hundred training runs per case, each trained for 100 epochs, to account for stochastic variations in the optimization process.

### 2.5. Dimensionality reduction and reconstruction POD-LSTM

The proposed methodology POD-LSTM with mesh deformation is shown in Fig. 4. A non-intrusive reduced dimension approach for high-dimensional flow field data is proposed. A data field is acquired with the state vector $\boldsymbol{s_i}(\boldsymbol{x}, \boldsymbol{t})$ as historical snapshot information through the Hi-Fi simulations around the airfoil. Then, the POD method is applied to extract the spatial modes $\phi_j(\boldsymbol{x}), j = 1, 2, \cdots, N_r^{s_i}$, which capture the essential dynamics of the flow and the wake together with the temporal coefficients that are determined from high to low order based on the energy of the spatial modes (Fig. 4). The low order modes represent the predominant flow and wake instabilities containing higher energy, whereas the high order modes highlight low energy (higher frequency) properties of smaller scale vortex structures. The temporal coefficients are predicted and extrapolated in time with the LSTM and Bi-LSTM models. The model reliability is critically assessed through their prediction error compared to the original data signal from Hi-Fi simulation fields. The reconstructed flow field with the multiplication of both spatial modes and the new predicted temporal coefficients results into a new prolongated Hi-Fi simulation up to the time $t_{pr}$ (Fig. 4). The simulation is then extrapolated in time considering all non-linear unsteady behaviour of the flow around the aerofoil, and the wake instabilities.

**Table 2**
Sensitivity study of various time steps for the mesh 3 regarding the time-average aerodynamic coefficients of lift and drag for unsteady simulations.

| | 5e-4 s | 1e-4 s | 5e-5 s | 1e-5 s | 5e-6 s |
|---|---|---|---|---|---|
| $\overline{CL}$ | 1.4808 | 1.4433 | 1.4211 | 1.4491 | 1.4484 |
| $\left\|\frac{\overline{CL}_{1e-5} - \overline{CL}_i}{\overline{CL}_{1e-5}} \times 100\right\|$ | 2.1923 | 0.7484 | 1.9285 | – | 0.1914 |
| $\overline{CD}$ | 0.0327 | 0.0321 | 0.0305 | 0.0292 | 0.0288 |
| $\left\|\frac{\overline{CD}_{1e-5} - \overline{CD}_i}{\overline{CD}_{1e-5}} \times 100\right\|$ | 11.7758 | 9.8889 | 4.4872 | – | 0.6163 |

## 3. Results

### 3.1. Verification of the Hi-Fi simulation model

The A320 wing prototype "Intermediate Scale – IS" of the BEALIVE project has been considered, having a chord of 0.70 m chord and span of 0.59 m length, the same dimensions as in the S4 wind tunnel of IMFT – Institut de Mécanique des Fluides de Toulouse where the "live-skin" morphing experiments are carried out. Regarding the mesh sensitivity, two-dimensional grids are constructed following the experimental S4 wind tunnel similar to its test section. The grids have been thoroughly studied in previous studies (Marouf et al., 2023). Reynolds number has been set to 1 million and the wing has been placed at an incidence angle of 10°.

The mesh sensitivity is presented in Table 1:

Regarding the mesh sensitivity, the difference in total cell count between Mesh 1 and Mesh 4 is 47%. The mesh refinement was not applied uniformly or arbitrarily. Instead, it was focused on the airfoil region and the wake. In particular, refinements were introduced in the first cell height, expansion ratio, and in the number of cells along both the horizontal and vertical directions.

All grids were compared to the finer grid (Mesh 4), and the relative error was calculated. This error decreases as the number of cells increases, reaching an error less than 1% for the lift coefficient and 0.34% for the drag coefficient. The Mesh 3 has been selected for further investigation. Given the significant influence of unsteady wake dynamics and the interactions of multi-frequency instabilities that enrich the energy spectra at this Reynolds number, it is essential to investigate the effect of the time step using an implicit dual-time stepping scheme. Table 2 presents the dependence of the time-averaged aerodynamic coefficients on the various time steps for Mesh 3. A time step ($dt$) of $1 \times 10^{-5}$ s compared to $5 \times 10^{-6}$ s yields errors of 0.19% and 0.62% for the lift and drag coefficients, respectively. The following time step has been selected for conducting unsteady simulations due to its optimal balance between simulation duration and CPU resources needed.

A test section identical to that used in the wind-tunnel experiments was selected to validate the numerical model with time-resolved PIV (TRPIV) measurements reported by (Jodin et al., 2017). The comparison is performed on time-averaged velocity fields obtained from both the experiments and the numerical simulations, as shown in Fig. 5.

The experimental measurements were conducted over a field of view of 14 014 pixels (143 × 98). The time-averaged velocity field reveals a good agreement between the experimental and numerical results in terms of velocity deficit magnitude, wake thickness, and downstream evolution of the wake. Both results exhibit a similar wake spreading rate and comparable recovery of the streamwise velocity along the centreline, indicating that the numerical model captures the main characteristics of the mean wake flow obtained experimentally.

Fig. 6 presents comparison of the longitudinal mean velocity profiles between the simulations and experiments. Overall, the numerical model provides a good agreement with the experiment. A slight overestimation of the velocity deficit is observed in the numerical results farther downstream, at $x/C = 1.15$ and $x/C = 1.20$.

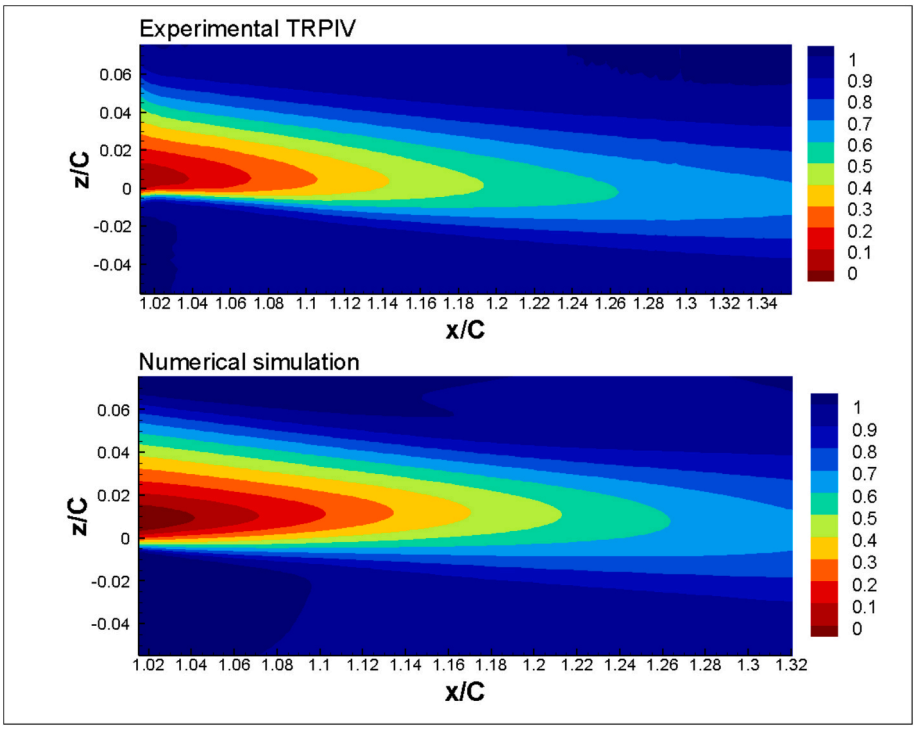


**Fig. 5.** Time-averaged velocity field in the near trailing-edge wake: comparison between experimental TR-PIV measurements (top) and two-dimensional numerical simulation (bottom).

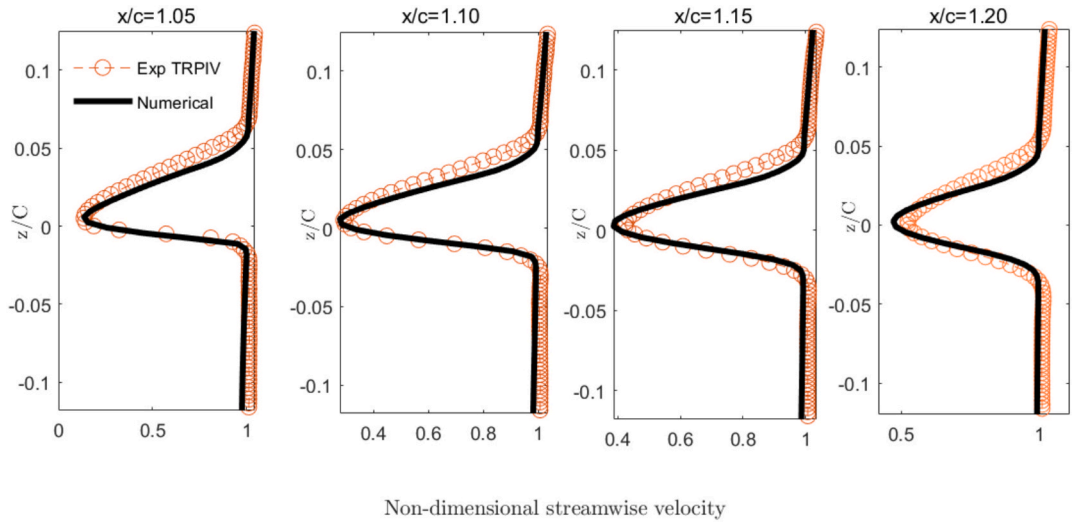


**Fig. 6.** Time-averaged velocity profiles along vertical lines in the near trailing-edge wake: comparison between experimental TR-PIV measurements and three-dimensional numerical simulations.

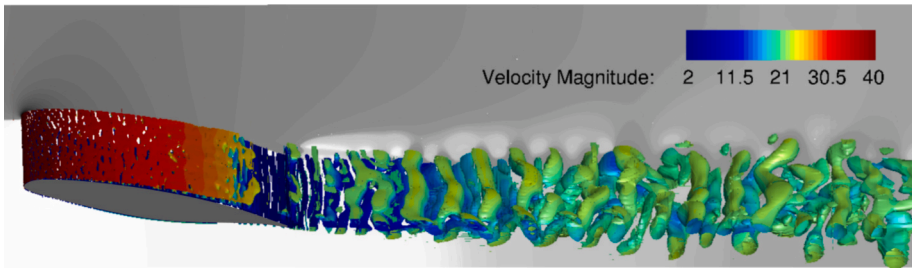


**Fig. 7.** Q criterion (=1000) *iso*-surfaces coloured with the velocity magnitude with a plane of pressure field with three-dimensional simulations.

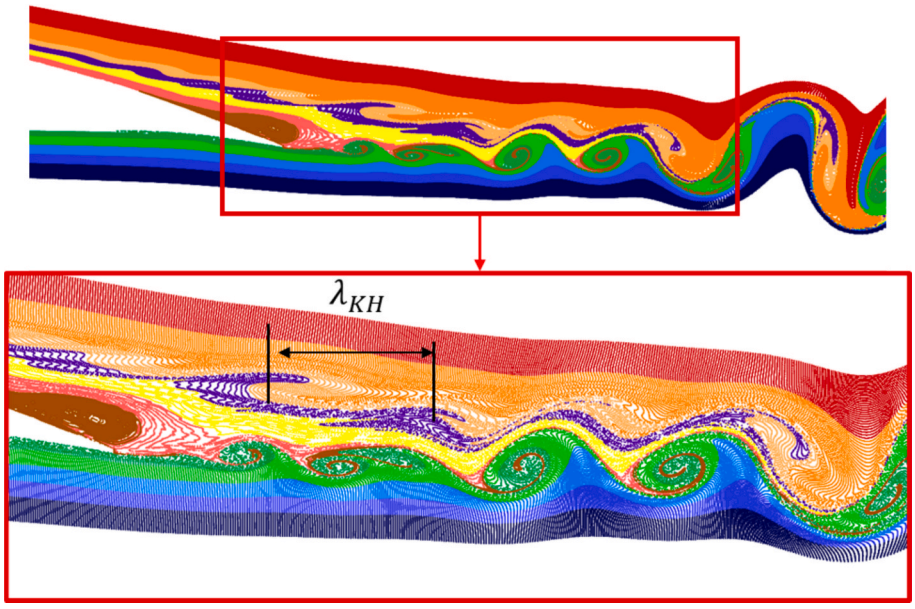


**Fig. 8.** Streaklines visualization showing the shear layer undulations, formation of Kelvin-Helmholtz vortices and von Kármán vortices, static (unactuated) case.

### 3.2. Flow and wake dynamics description

As seen in Fig. 7, the Hi-Fi simulations can produce the physical flow structures involving the separation area, the upper and lower shear layers development with the Kelvin-Helmholtz vortex structures producing farther downstream the alternating von Kármán vortex pattern, following the amplification of the related flow instabilities. Furthermore, the model provides the spanwise undulation of these vortex rows, following the secondary instability, as in DNS by Braza et al. (Braza et al., 2001). Main flow instabilities such as near trailing edge boundary layer separation are shown in Fig. 7 and an appearance of the upper and lower shear layer instabilities with von Kármán vortices developed further in the wake.

According to the discussion in this section, the present Hi-Fi modelling has been validated in respect of its ability to capture the 3D flow dynamics that is essential for the evaluation of the aerodynamic forces. The LSTM model ability to provide a training and extension of the time solution is reliable under the condition that the Hi-Fi data base contains the main flow physics correctly. A comparison to other turbulence models can be found in (Marouf, 2020), where it was shown that they failed to predict correctly the flow separation and consequently, the development of the related instabilities and coherent structures in the wake. These limitations that significantly impacts the accuracy of aerodynamic force predictions.

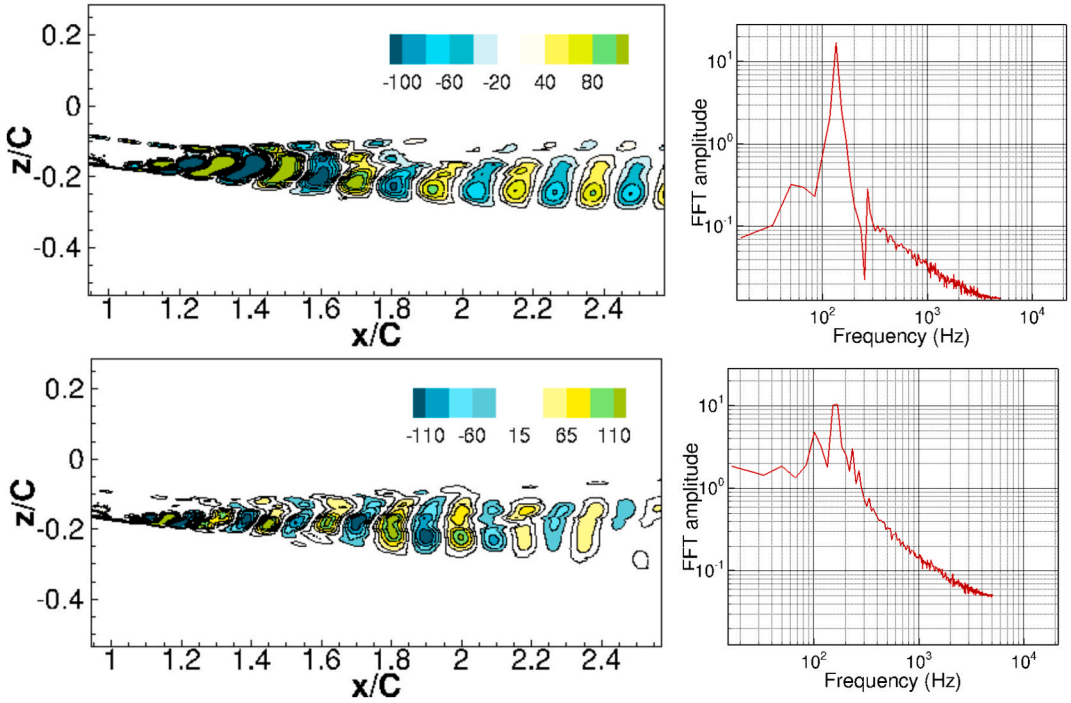


**Fig. 9.** Decomposed POD spatial modes and FFT of temporal modes. (top): mode 2. (down): mode4. (left): vorticity computed from spatial modes. (right): FFT of temporal coefficients related to the modes.

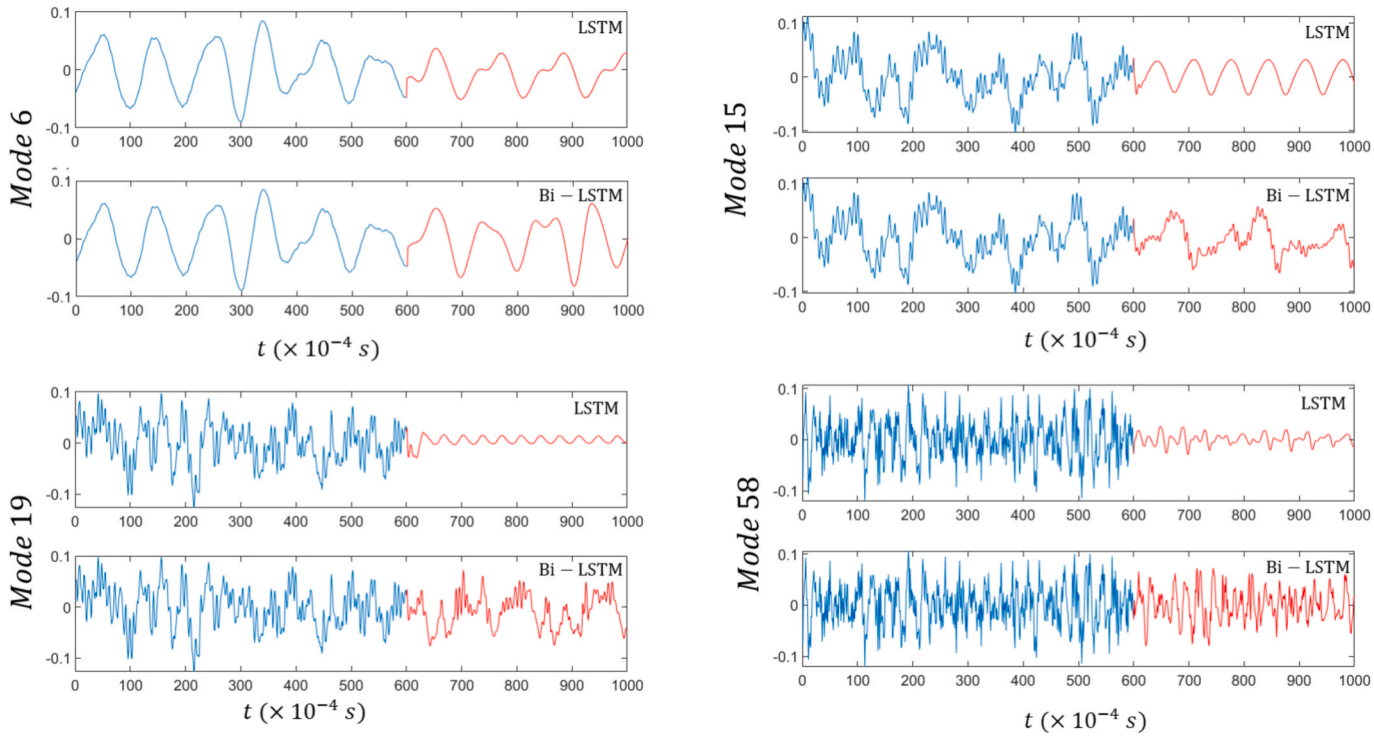


**Fig. 10.** Temporal POD coefficients: comparison between high-fidelity data $(1-600) \times 10^{-4}s$ and predictions obtained using LSTM and bidirectional LSTM (Bi-LSTM) models (601–1000) $\times\ 10^{-4}s$.

Fig. 8 presents streaklines visualization of the wake through a zoomed view of the near trailing-edge region and of the wake illustrating the shear layer undulation that creates Kelvin-Helmholtz (KH) vortices, as well as the alternating vortex shedding with the von Kármán vortices farther downstream. The wavelength $\lambda_{KH}$ of the upper shear layer downstream of the separation area has been estimated to be 8–10% of the airfoil's chord. The upper shear layer is characterised by a predominant frequency, $f_{USL}$ in the range of (195–200) Hz. The lower shear layer frequency, $f_{LSL}$ is of 240 Hz. The natural shedding frequency of the von Kármán vortices, $f_{vK}$ is in the order of 160 Hz. The above frequencies have been identified from detailed from tracking of the coherent vortices according to a detailed exploitation of the numerical flow visualisation instantaneous fields whose an example is presented in Fig. 8. These frequency peaks appear as predominant bumps and not all as sharp peaks due to the interaction with the chaotic turbulence that produces a slight "smearing" of these frequencies around the aforementioned values.

### 3.3. POD and machine learning analysis for the non-actuated case (static) case

The POD analysis has been performed on Hi-Fi simulations using instantaneous velocity fields $(\boldsymbol{U_x}, \boldsymbol{U_z})$, through 600 snapshots, collected at a time interval of $\Delta t = 10^{-4}$s. The resulting spatial modes and

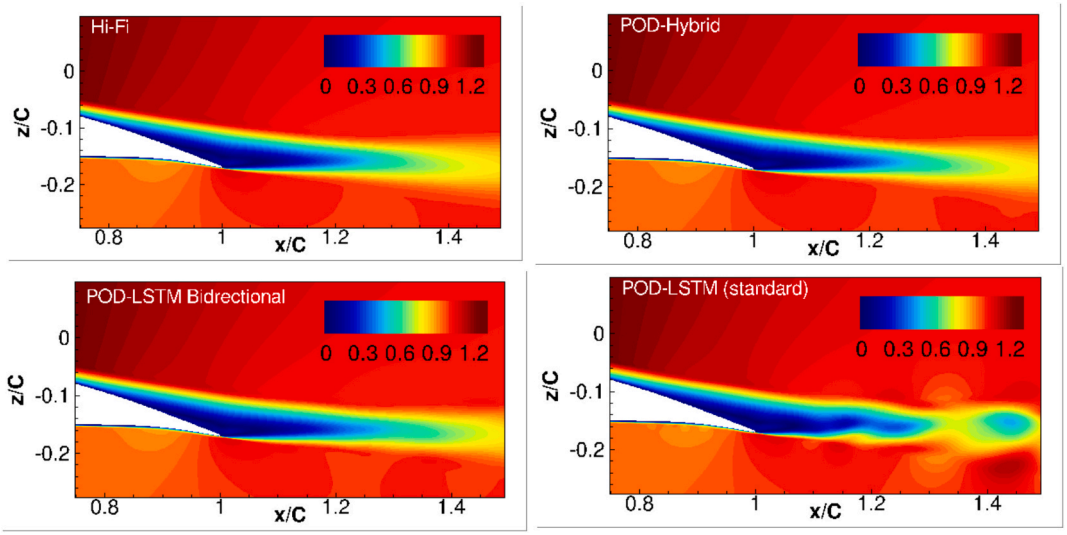


**Fig. 11.** Time-averaged non-dimensional velocity magnitude comparison between High-Fidelity simulations, LSTM (standard), LSTM-Bidirectional and the Hybrid model.

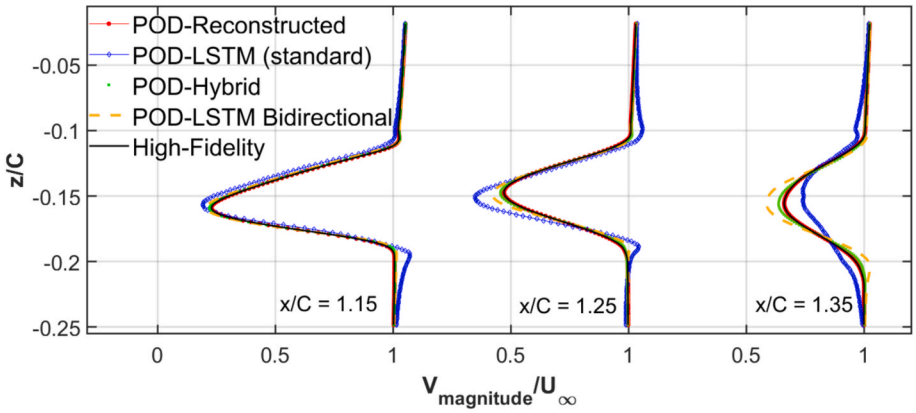


**Fig. 12.** Time-averaged non-dimensional velocity magnitude extracted along different locations in the near wake region.

temporal coefficients have been computed and ranked according to their energy content. Fig. 9(left) presents the vorticity field ($\omega_y$) reconstructed from the spatial modes derived from the velocity data for mode 2 (top) and 4 (bottom) respectively.

The spatial modes 2 and 4 exhibit significant energy associated with counter-rotating vortices within the region between $x = 1.1$ and $x = 1.6$. This is attributed to predominant frequencies of both the shear layer and the von Kármán vortices. A Strouhal number based on the wing chord in the range of (10–11) corresponds to the primary instability of the shear layer which develops in the near-wake region (in agreement with the experimental study and POD of (Jodin et al., 2017), while a lower Strouhal number in the range (3–4) is associated with the von Kármán vortices, which form further downstream in the wake.

Fig. 10, shows the comparison between the LSTM and Bi-LSTM model where the POD temporal coefficients signals are presented.

The Bi-LSTM demonstrates superior performance in predicting the temporal evolution of POD coefficients (Fig. 10). This is consistent with previous findings reported in (Graves et al., 2005), where the Bi-LSTM outperformed the standard LSTM and other recurrent neural network architectures.

The present signals are characterised by a rich frequency content due to the turbulence fluctuations at Reynolds number of 1 Million. For low-frequency signals, the standard LSTM performs adequately, offering similar accuracy with reduced training time and lower model complexity.

The hybrid model proposed here combines the strengths of both approaches: for each predicted temporal coefficient, the outputs from the LSTM and Bi-LSTM models are compared, and the signal with the lower prediction loss is selected. This strategy ensures that the best prediction is retained for each mode while minimizing the overall error.

The POD decomposition providing these various modes with their related energy allows the LSTM model to directly predict each mode from high energy with coherent vortices to low energy chaotic small-scale vortices, while maintaining the correct energy transfer between them.

The time-averaged dimensionless velocity field has been computed from the Hi-Fi simulations and from the POD reconstructions using two LSTM architectures namely, the LSTM (standard) and LSTM-Bidirectional. Furthermore, the present study has developed a *Hybrid model* (Fig. 11) that selects the best predictions with the minimum loss error from the LSTM (standard) and the LSTM-Bidirectional model.

The hybrid model shows very good agreement with the Hi-Fi simulation. It accurately captures the velocity deficit associated with the separated boundary layer, as well as the evolution of both the upper and lower shear layers and the wake development. The POD-Bidirectional model slightly overestimates the wake deficit, particularly in the region $x/C \in [1.25,1.35]$.

The POD-LSTM (standard) model fails to reproduce the averaged

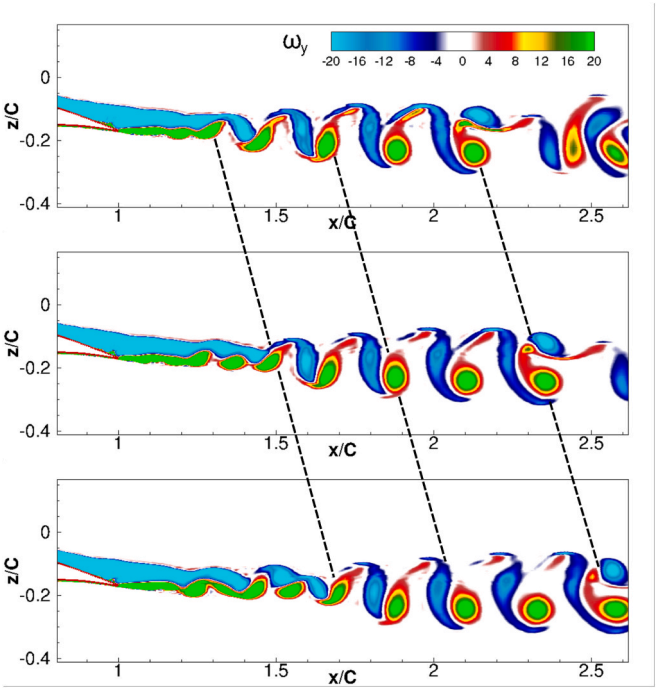


**Fig. 13.** *Iso*-vorticity for the predicted reconstructed solution with POD-Hybrid method, (top): $t^* = 20.05$ (0.653 s), (middle): $t^* = 21.90$ (0.713 s) and (down): $t^* = 24.72$ (0.803 sec).

velocity field correctly, Fig. 11. The velocity field shows fluctuations and a discontinuity in the velocity deficit around x/C = 1.3, indicating that the spatio-temporal evolution of the wake has not been properly reconstructed. The LSTM (standard) model, due to its relatively simple architecture, demonstrated limited capability in accurately predicting the temporal signals that exhibit shifts across frequency bands.

To better compare the efficiency of these different models, the mean longitudinal velocity is presented in various vertical positions, at x/C = 1.15, 1.25 and 1.35 along the vertical axis z/C axis (Fig. 12). At x/C = 1.15, all models are in good agreement in the velocity deficit. However, the LSTM (standard) shows an acceleration on the lower shear layer. Downstream in the wake, at x/C = 1.25 the LSTM (standard) over-predicts the velocity deficit and both inflection points are deviated from the Hi-Fi solution. The Bidirectional LSTM model also shows also an over-estimation of the velocity deficit. At x/C = 1.35, only the hybrid model maintains a good prediction of the wake velocity, the LSTM (standard) showing an increase of the velocity (seen also in the previous figure). Moreover, the Bidirectional LSTM tends to over-estimate the

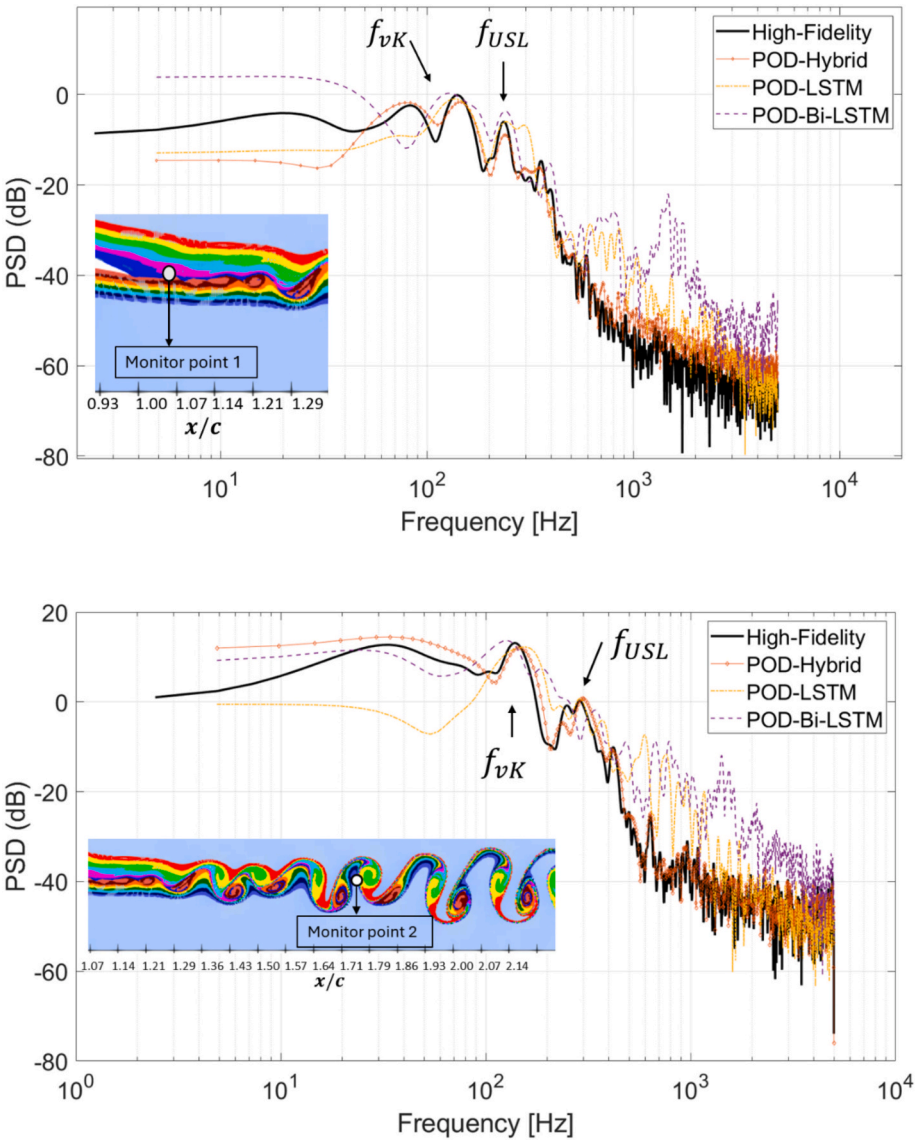


**Fig. 14.** PSD of crossflow velocity ($U_Z$) with the flow dynamics in the near wake and farther downstream. $f_{vK}$ and $f_{USL}$ correspond to the von Kármán and upper shear layer natural frequencies respectively. A comparison between High-Fidelity simulation and predictive models of POD with Machine Learning.

velocity.

The overall time-averaged velocity magnitude shows that the hybrid model demonstrates good results relative to High-Fidelity simulations. The relative error, calculated as follows $\frac{|\overline{U}_{\text{Hybrid}} - \overline{U}_{\text{High-fidelity}}|}{\overline{U}_{\text{High-fidelity}}} \times 100\%$, was evaluated for the hybrid model, which selects the best predictions between LSTM and Bidirectional LSTM. The maximum error was found to be below 3% for the overall time-averaged velocity.

Fig. 13 shows the ability of the Hybrid model in predicting the unsteady flow dynamics by the reconstruction of the extended temporal and spatial coefficients. The contours of the vorticity $\omega_y$ are shown for various times according to this model. It has been shown that the hybrid model has been able to reconstruct the upper and lower shear layers and their interactions. The weak undulation of the shear layers near the trailing edge region according to the related shear layer instability in the near wake, presenting small amplitude oscillations or waviness and leading to formation of Kelvin Helmholtz (KH) vortices dominating the initial growth of the shear-layer, is illustrated. Achieving critical amplitudes, the KH begins to roll up into discrete vortical structures (larger coherent structures), where the first "vortex core" is visible near $x/C = 1.4 - 1.6$. Each side of the shear layer sheds alternating vortices of opposite sign. This interaction produces the von Kármán street regime from $x/C = 1.5 - 2.5$. The formation of the von Kármán vortex shedding, and the development of the wake which tends to expand also in the crossflow direction with a constant shedding frequency are obtained. These vortices are advected in the spatio-temporal framework properly. The convection of these coherent structures has been well respected through the Hybrid model (Fig. 13). Therefore, the POD-ML hybrid model is able to capture the wake unsteadiness by limiting the numerical diffusion and dissipation.

Fig. 14 show the Power Spectral Density (PSD) at two monitor points, one in the near wake and another further downstream, with all models compared to high-fidelity simulations. The models capture the main predominant frequency bumps and peaks associated with the dynamics of the coherent structures, such as the von Kármán vortices and the Kelvin-Helmholtz (KH) vortices in the upper and lower shear layers. Both LSTM and Bi-LSTM tend to overpredict the amplitude (energy) of smaller-scale, high-frequency (chaotic) structures. The Hybrid model exhibits excellent agreement with the high-fidelity simulation across the full frequency spectrum.

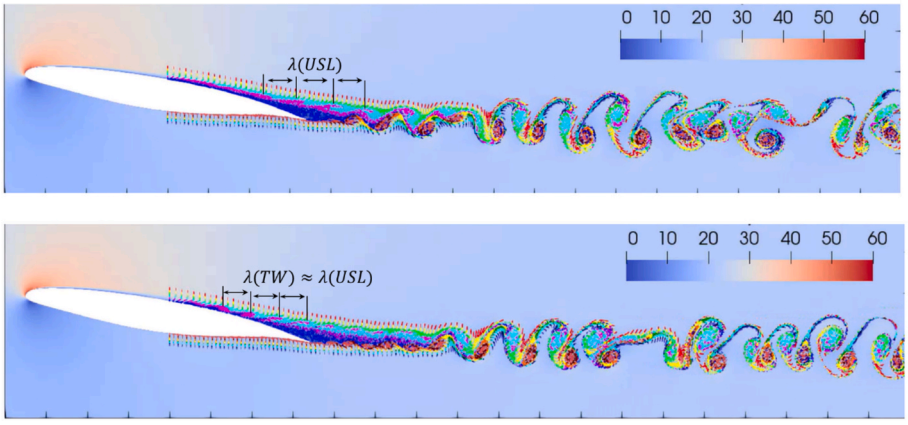


**Fig. 15.** Instantaneous streaklines visualization with, in background, the field of streamwise velocity for the static case (top) and the morphing case (bottom).

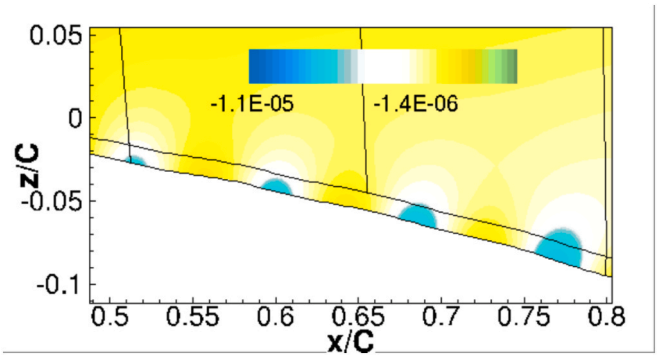


**Fig. 16.** The new mode 2 related to the vertical deformation computed from the pod.

### 3.4. POD and machine learning analysis for the actuated case (travelling wave)

In this section, the POD is extended to the morphing case with an imposed Traveling Wave (TW) in the region between 30% of the chord up to the trailing-edge, with an imposed amplitude (A) of 0.15% of the total chord. The wavelength ($\lambda$) is set at 8.5% of the total chord and the frequency actuation is fixed at 300 Hz.

Fig. 15 compares the static case with the morphing case employing a travelling wave (TW) actuation. In the morphing case, the wavelength of the travelling wave, $\lambda_{TW}$, is close to the frequency of the upper shear layer, $\lambda_{USL}$. This proximity induces a coupling between the TW wavelength and the one of the natural upper shear layer frequency (also shown in Fig. 8), resulting in a lock-in phenomenon where the wavelength of the upper shear layer is close to the one imposed by the actuation. This reinforces the regularity of the USL creating a longer formation region than in the static case. Consequently, the formation of the von Kármán vortex shedding is swept farther downstream and the near wake's width is reduced, thus enhancing an overall drag reduction and improves the aerodynamic efficiency.

The POD in the present case accounts for the variation in the mesh deformation due to the imposed displacement. This deformation is included into the snapshot matrix, where the grid coordinates are involved as a variable, together with the velocity components. The additional relevant modes associated with the grid deformation are now calculated together with the modes corresponding to the velocity components $U_x$ and $U_z$.

The newly identified modes are linked to the deformation of the TW surface. Fig. 16 illustrates the crossflow deformation for mode 2, highlighting both upward and downward displacements of the advected surface wave. Modes $U_x$ and $U_z$ describe flow-dominated instabilities that arise as a combination of natural instabilities of the predominant shear-layer regime presented by the mode 4 (Fig. 17). These instabilities are manipulated through the TW actuation, shown having a high energy along the suction side of the wing. Counter rotating vortices are captured by the vorticity ($\omega_y$) containing high energy due to the interaction of the TW and the upper shear layer. Therefore, the POD-Mesh

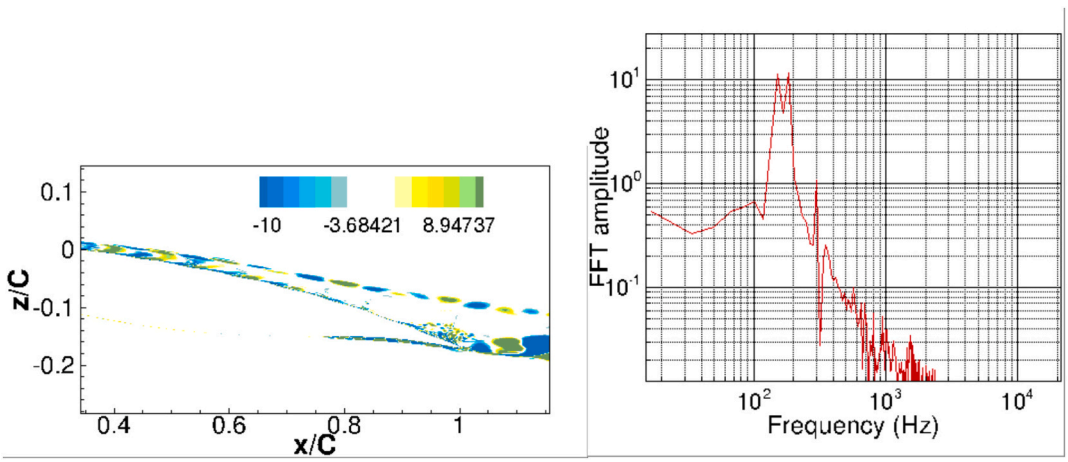


**Fig. 17.** Spatial mode 4 and fft of the temporal coefficient. the mode shows the tw effect on the upper shear layer and its signature on the fft with the actuation frequency at 300 Hz (St = 9.76).

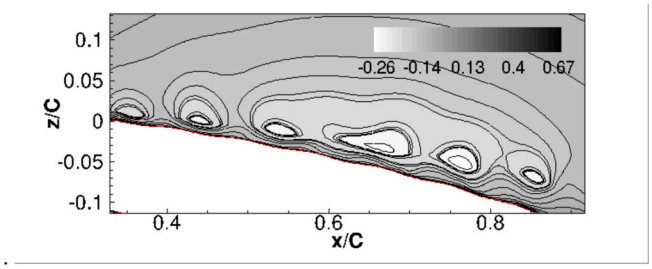


**Fig. 18.** Reconstructed POD of the non-dimensional instantaneous crossflow velocity ($U_z$) in the suction side of the airfoil.

has been able to capture these effects due to the imposed spatio-temporal deformation considered in the POD snapshot.

The reconstruction of the POD shows the correct deformation of the wall as presented in Fig. 18. The non-dimensional crossflow velocity shows the effect of the Travelling Wave by imposing not only an advective velocity to the streamflow velocity but also by injected small-scale turbulent structures inside the upper shear layer. It consists of the coupling between the imposed wavelength of the TW and the one of the upper shear-layer. These structures modify the near wake vortices downstream.

These effects are well captured by the POD-reconstruction and furthermore the predicted POD-Mesh-ML models.

To evaluate the accuracy of the developed model various monitor points are extracted from the wake presented by the instantaneous non-dimensional crossflow velocity ($U_z/U_\infty$) (Fig. 19 (left)). The non-dimensional streamflow velocity ($U_x/U_\infty$) is presented in Fig. 19 (right) for both reconstructed POD in the non-dimensional time (reinitialized) range [0–2] and predicted POD-Mesh-ML model [2–3]. The predicted model shows a similar behaviour of amplitudes and frequencies to the Hi-Fi model in different regions of the wake from near trailing edge up to 1.8C further downstream. These figures illustrate the ability of the hybrid model to capture both, higher frequency dynamics in the near trailing-edge region due to the KH vortices formation and the lower frequency dynamics dominant farther downstream in the wake due to the VK mode.

## 4. Conclusion

The study proposes a new approach to predict turbulent flow dynamics in the context of fluid–structure interaction produced from surface deformation through morphing. The application concerns Hi-Fi simulations involving Travelling Waves (TW) on the suction side of the "Intermediate Scale – IS" A320 morphing prototype of the HORIZON-2023–2027-PATHFINDER Project N° 101129952-BEALIVE-"Bioinspired Electroactive multiscale Aeronautical Live skin", https://horizon

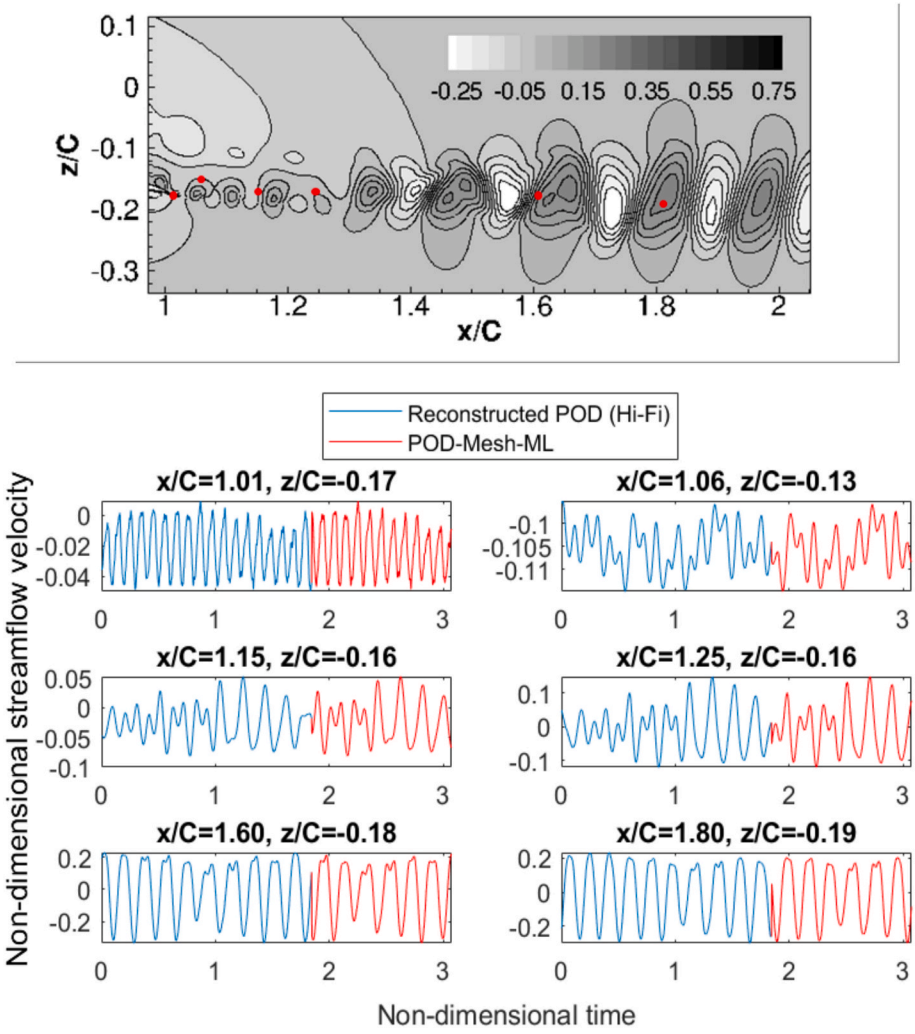


**Fig. 19.** (Top) Hi-Fi dimensionless instantaneous crossflow velocity ($U_z$) in the wake region with chosen extracted monitor points. (Bottom) illustrating the dimensionless streamflow velocity ($U_x$). The blue coloured signals refer to the reconstructed POD and the red coloured are the prediction with the Hybrid model. (For interpretation of the references to colour in this figure legend, the reader is referred to the web version of this article.)

-europe-bealive.eu/.

A Reduced Order Modelling methodology has been developed based on LSTM NNs training of the POD temporal coefficients to extend the duration of the Hi-Fi solution that is time consuming in terms of CPU. on the purpose to increase the optimum design cycles in realistic times and by involving the complex unsteady flow dynamics appearing in the high Reynolds number range due to turbulence, towards enabling near real scale design. The study employs the POD methodology that allows reduction of the principal temporal and spatial modes governing the dynamic system in the range of high and moderate energy modes. In this article, the POD is extended to a deforming mesh and coupled with the LSTM methodology.

To this end, Hi-Fi simulations have been first provided with appropriate turbulence modelling able to capture the instabilities development and the dynamics of the related coherent structures around the wing. These simulations have been performed in two and three dimensions at Reynolds number of 1 million, Mach number of 0.06 and angle of incidence of 10°, corresponding to take-off conditions in the low subsonic regime.

The results provided the ability of extending the Hi-Fi solution through training of the POD temporal coefficients by means of the LSTM model and reconstruction afterwards by considering a significant number of low order modes representing the main dynamics around the wing.

A critical assessment of the LSTM and the Bi-LSTM training has been addressed in comparison with the Hi-Fi simulation. A hybrid model associating both the standard and the bidirectional LSTM has been developed. The superiority of this model in correctly capturing the flow dynamics compared to the Hi-Fi simulations has been demonstrated for the unactuated (static case) and the morphing case through travelling waves applied on a specific area of the suction side of the A320 morphing prototype by saving CPU time considerably.

The effects of the deformation of the suction side surface in respect of the travelling wave on the flow dynamics has been also accurately predicted in comparison to the Hi-Fi simulations through the POD-Mesh-ML model involving the grid deformation as a principal variable in the POD correlation matrix in addition to the velocity component variables and trained in the POD process through the LSTM.

The present article offers a new approach for fast prediction of unsteady flows without the need for a large database to train the model. The approach can be implemented in real time simulations.

As a direct perspective in the ongoing developments of the research team involved in this study, the pressure coefficients variable is also included in the POD to allow the prediction of the aerodynamic forces. Therefore, optimisation regarding the aerodynamic efficiency increase through the morphing and the present hybrid model is under investigation with reduced simulation time.

## CRediT authorship contribution statement

**Abderahmane Marouf:** Writing – review & editing, Software, Methodology, Conceptualization. **Nils Maynard:** Writing – review & editing, Methodology, Conceptualization. **Rajaa El Akoury:** Writing – review & editing, Methodology, Conceptualization. **Jean-François Rouchon:** Writing – review & editing, Supervision, Resources, Methodology. **Yannick Hoarau:** Writing – review & editing, Supervision, Software, Resources, Methodology, Conceptualization. **Marianna Braza:** Writing – review & editing, Supervision, Resources, Project administration, Methodology, Funding acquisition, Conceptualization.

## Declaration of competing interest

The authors declare that they have no known competing financial interests or personal relationships that could have appeared to influence the work reported in this paper.

## Acknowledgements

The present study has been funded by the European Commission HORIZON-2023-2027-PATHFINDER Project N° 101129952-BEALIVE-"Bioinspired Electroactive multiscale Aeronautical Live skin", http://horizon-europe-bealive.eu/.

Part of the study has been funded by the French "Agence Nationale de recherche - ANR" project EMBIA (https://anr.fr/Projet-ANR-21-CE05-0006). The authors like to acknowledge the High-Performance Computing Center of the University of Strasbourg for supporting this work by providing scientific support and access to computing resources. The computing resources were funded by the Equipex Equip@Meso project (Programme Investissements d'Avenir) and the CPER Alsacalcul/Big Data. The authors are grateful to the French supercomputing Centres CINES, TGCC and CALMIP for having provided a considerable CPU allocation: DARI-GENCI:Grant 2025-A0192A16870 for the University of Strasbourg and 2025-A0182A05140 for the Institut de Mécanique des Fluides de Toulouse (IMFT), as well as the considerable CPU allocation of the CALMIP Supercomputing Centre (project P0044) to IMFT.

## Data availability

No data was used for the research described in the article.

## References

Abadi, M., et al., 2016. TensorFlow: Large-Scale Machine Learning on Heterogeneous Distributed Systems. CoRR, abs/1603.04467. https://arxiv.org/abs/1603.04467.

Abou Khalil, J., Jiménez Navarro, C., El Jeaid, R., Marouf, A., El Akoury, R., Hoarau, Y., Rouchon, J.-F., Braza, M., 2024. Aerodynamic performance increase over an A320 morphing wing in transonic regime by numerical simulation at high Reynolds number. J. Numer. Methods Heat Fluid Flow. https://doi.org/10.1108/HFF-12-2023-0758.

Bar-Sinai, Y., Hoyer, S., Hickey, J., Brenner, M.P., 2019. Learning data-driven discretizations for partial differential equations. Proc. Natl. Acad. Sci. 116 (31), 15344–15349.

Bourguet, R., Braza, M., Harran, G., Akoury, R.E., 2008. Anisotropic Organised Eddy simulation for the prediction of non-equilibrium turbulent flows around bodies. J. Fluids Struct. 24 (8), 1240–1251. https://doi.org/10.1016/j.jfluidstructs.2008.07.004.

Beck, A.D., Flad, D.G., Munz, C.-D., 2019. Deep neural networks for data-driven LES closure models. J. Comput. Phys. 398, 108910.

Braza, M., Perrin, R., Hoarau, Y., 2006. Turbulence properties in the cylinder wake at high Reynolds number. J. Fluids Struct. 22, 757–771. https://doi.org/10.1016/j.jfluidstructs.2006.04.021.

Braza, M., Faghani, D., Persillon, H., 2001. The role of natural vortex dislocations in three-dimensional wake transition. J. Fluid Mech. 439, 1–41.

Chollet, F., et al., 2018. Keras: The Python Deep Learning Library. Astrophysics Source Code Library, ascl:1806.022. https://github.com/keras-team/keras.

Deng, Z., Chen, Y., Liu, Y., Kim, K.C., 2019. Time-resolved turbulent velocity field reconstruction using a long short-term memory (LSTM)-based artificial intelligence framework. Phys. Fluids 31, 075108.

Donea, J., Giuliani, S., Halleux, J.P., 1982. An arbitrary lagrangian-eulerian finite element method for transient dynamic fluid-structure interactions. Comput. Methods Appl. Mech. Eng. 33 (1), 689–723. https://doi.org/10.1016/0045-7825(82)90128-1.

Du, J., Li, X., Dong, S., Liu, Z., Chen, G., 2024. A novel attention-enhanced deep neural network for hypersonic spatiotemporal turbulence prediction. Phys. Fluids 36 (5), 055145. https://doi.org/10.1063/5.0210966.

Eivazi, H., Tahani, M., Schlatter, P., Vinuesa, R., 2022. Physics-informed neural networks for solving Reynolds-averaged Navier–Stokes equations. Phys. Fluids 34 (7), 075117. https://doi.org/10.1063/5.0095270.

El Akoury, R., Marouf, A., Abou Khalil, J., Hoarau, Y., Rouchon, J.F., Braza, M. 2024. Numerical investigation of electroactive morphing effects through traveling wave actuation on an A320 wing in low subsonic regime and Reynolds number of 1 million. 9th ECCOMAS Invited Special technology Session -STS 247 "Disruptive Aircraft's Wing Configurations towards Greening of Aviation" - invited, Book of abstracts, Lisbon 3-7 June 2024.

Favre, A., 1983. Turbulence: Space-time statistical properties and behavior in supersonic flows. Phys. Fluids 26 (10), 2851–2863. https://doi.org/10.1063/1.864049.

Graves, A., Fernández, S., Schmidhuber, J. (2005). Bidirectional LSTM Networks for Improved Phoneme Classification and Recognition. In: Duch, W., Kacprzyk, J., Oja, E., Zadrożny, S. (eds) Artificial Neural Networks: Formal Models and Their Applications – ICANN 2005. ICANN 2005. Lecture Notes in Computer Science, vol 3697. Springer, Berlin, Heidelberg. https://doi.org/10.1007/11550907_126.

Hoarau, Y., 2002. Analyse physique par simulation numérique et modélisation des écoulements décollés instationnaires autour de surfaces portantes. Thèse de doctorat, Université de Strasbourg.

Hochreiter, S., Schmidhuber, J., 1997. Long short-term memory. Neural Comput. 9 (8), 1735–1780. https://doi.org/10.1162/neco.1997.9.8.1735.

Jameson, A., 1993. Artificial diffusion, upwind biasing, limiters and their effect on accuracy and multigrid convergence in transonic and hypersonic flows. in *Proceedings of the AIAA 11th Computational Fluid Dynamics Conference*, Orlando, USA, pp. 1-28. https://doi.org/10.2514/6.1993-3359.

Jodin, G., Motta, V., Scheller, J., Duhayon, E., Döll, C., Rouchon, J.F., Braza, M., 2017. Dynamics of a hybrid morphing wing with active open loop vibrating trailing edge by time-resolved PIV and force measures. J. Fluids Struct. 74, 263–290. https://doi.org/10.1016/j.jfluidstructs.2017.06.015.

Kutz, J.N., 2017. Deep learning in fluid dynamics. J. Fluid Mech. 814, 1–4.

Lapeyre, C.J., Misdariis, A., Cazard, N., Veynante, D., Poinsot, T., 2019. Training convolutional neural networks to estimate turbulent sub-grid scale reaction rates. Combust. Flame 203, 255.

Li, Z., Kovachki, N., Azizzadenesheli, K., Liu, B., Bhattacharya, K., Stuart, A., & Anandkumar, A., 2020. Fourier neural operator for parametric partial differential equations. arXiv preprint arXiv:2010.08895.

Ling, J., Kurzawski, A., Templeton, J., 2016. Reynolds averaged turbulence modelling using deep neural networks with embedded invariance. J. Fluid Mech. 807, 155–166.

Lumley, J.L., 1967. The structure of inhomogeneous turbulent flows. In Atmospheric Turbulence and Radio Wave Propagation: Proceedings of the International Colloquium, Nauka, Moscow, Jun, pp. 167–178.

Marouf, A., 2020. Analyse physique de concepts du morphing éléctroactif pour accroître les performances aérodynamiques des ailes du futur par simulation numérique de Haute-Fidélité et modélisation de la Turbulence a nombre de Reynolds élevé. Université de Strasbourg. PhD thesis.

Marouf, A., Bmegaptche Tekap, Y., Simiriotis, N., Tô, J.-B., Rouchon, J.-F., Hoarau, Y., Braza, M., 2021. Numerical investigation of frequency-amplitude effects of dynamic morphing for a high-lift configuration at high Reynolds number. Int. J. Numer. Meth. Heat Fluid Flow 31 (2), 599–617. https://doi.org/10.1108/HFF-07-2019-0559.

Marouf, A., Hoarau, Y., Rouchon, J.-F., Braza, M., 2023. Three-dimensional simulation effects of trailing-edge actuation on a morphing A320 wing by means of hybrid turbulence modelling. Int. J. Numer. Meth. Heat Fluid Flow 33 (4), 1436–1457. https://doi.org/10.1108/HFF-09-2022-0559.

Marouf, A., Braza, M., Hoarau, Y., 2025. A comparative study of correlation-based transition models for aerodynamics in CFD code NSMB. In: Zeidan, D., Hidalgo, A., Zhang, L.T., Goncalves Da Silva, E. (Eds.), Computational Fluid Dynamics: Novel Numerical and Computational Approaches. Springer, Singapore. https://doi.org/10.1007/978-981-97-8152-2_5.

Mohan, A.T., Gaitonde, D.V., 2018. A deep learning-based approach to reduced order modeling for turbulent flow control using LSTM neural networks. arXiv preprint arXiv:1804.09269.

Maulik, R., Lusch, B., Balaprakash, P., 2021. Reduced-order modeling of advection-dominated systems with recurrent neural networks and convolutional autoencoders. Phys. Fluids 33 (3), 037106. https://doi.org/10.1063/5.0039986.

Poinsot, T.J., Lele, S.K., 1992. Boundary conditions for direct simulations of compressible viscous flows. J. Comput. Phys. 101 (1), 104–129. https://doi.org/10.1016/0021-9991(92)90046-2.

Simiriotis, N., Jodin, G., Marouf, A., Elyakime, P., Hoarau, Y., Hunt, J.C.R., Rouchon, J. F., Braza, M., 2019. Morphing of a supercritical wing by means of trailing edge deformation and vibration at high Reynolds numbers: experimental and numerical investigation. J. Fluids Struct. 91, 102676. https://doi.org/10.1016/j.jfluidstructs.2019.06.016.

Sirovich, L., 1987. Turbulence and the dynamics of coherent structures. I. Coherent structures. Quart. Appl. Math. 45 (3), 561–571.

Stevens, B., Colonius, T., 2020a. Enhancement of shock-capturing methods via machine learning. Theor. Comput. Fluid Dyn. 34, 483–496.

Stevens, B., Colonius, T., 2020b. Finitenet: A fully convolutional LSTM network architecture for time-dependent partial differential equations. arXiv preprint arXiv: 2002.03014.

Szubert, D., Grossi, F., Jimenez-Garcia, A., Hoarau, Y., Hunt, J.C.R., Braza, M., 2015. Shock-vortex shear-layer interaction in the transonic flow around a supercritical airfoil at high Reynolds number in buffet conditions. J. Fluids Struct. 55, 276–302. https://doi.org/10.1016/j.jfluidstructs.2015.03.005.

Tô, J.-B., Simiriotis, N., Marouf, A., Szubert, D., Asproulias, I., Zilli, D.M., Hoarau, Y., Hunt, J.C.R., Braza, M., 2019. Effects of vibrating and deformed trailing edge of a morphing supercritical airfoil in transonic regime by numerical simulation at high Reynolds number. J. Fluids Struct. 91, 102595. https://doi.org/10.1016/j.jfluidstructs.2019.02.011.

Truong, H., Marouf, A., Gehri, A., Vos, J., Braza, M., Hoarau, Y., 2023. Numerical investigation of active flow control using zero-net-mass-flux jets around a high-lift morphing cambered wing-flap system. Int. J. Numer. Meth. Heat Fluid Flow 33 (4), 1475–1488. https://doi.org/10.1108/HFF-09-2022-0558.

Vos, J., Rizzi, A., Corjon, A., Chaput, E., Soinne, E., 1998. Recent advances in aerodynamics inside the NSMB (Navier Stokes Multi Block) consortium. In 36th AIAA Aerospace Sciences Meeting and Exhibit. https://doi.org/10.2514/6.1998-225.

Zandalinas, S.I., Fritschi, F., Mittler, R., 2021. Global warming, climate change, and environmental pollution: recipe for a multifactorial stress combination disaster. Trends Plant Sci. 26 (6), 588–599. https://doi.org/10.1016/j.tplants.2021.02.011.

Zhang, J., Zhao, X., 2020. A novel dynamic wind farm wake model based on deep learning. Appl. Energy 277, 115552.